ACS OMEGA

http://pubs.acs.org/journal/acsodf

Article

Two-Dimensional Hexagonal-Shaped Mesoporous Carbon Sheets for Supercapacitors

Yafen Tian, Xiangyu Zhu, Muhammad Abbas, Daniel W. Tague, John P. Ferraris, and Kenneth J. Balkus, Jr.*

Cite This: *ACS Omega* 2022, 7, 27896−27902

Read Online

ACCESS | Metrics & More | Article Recommendations | Supporting Information

ABSTRACT: Two-dimensional mesoporous hexagonal carbon sheets (MHCSs) have been prepared via a chemical vapor deposition method employing mesoporous $Mg(OH)_2$ hexagonal sheets as the template and acetylene gas as the carbon precursor. MHCSs with porosity in the micropore−mesopore range have a high specific surface area of 1785 $m^2 \cdot g^{-1}$. The hierarchical microporous−mesoporous pore structure enables rapid ion transport across the hexagonal carbon sheets, resulting in superior electrochemical performance. The MHCS electrodes showed a maximum specific capacitance of 162 $F \cdot g^{-1}$ at 5 mV s^{-1} using the electrolyte 1-ethyl-3-methylimidazolium bis(trifluoromethylsulfonyl)imide (EMIM-TFSI). MHCS symmetric coin cells exhibited a maximum energy density of 67 $Wh \cdot kg^{-1}$ at 0.5 $A \cdot g^{-1}$ and a maximum power density of 14.97 $kW \cdot kg^{-1}$ at 10 $A \cdot g^{-1}$.

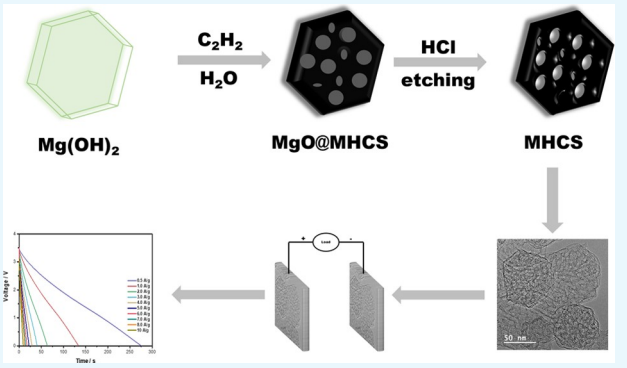

1. INTRODUCTION

The electric double layer capacitors (EDLCs) are attractive sources of energy for portable electronics, electric vehicles, and intelligent power networks. EDLCs work by rapidly generating a double layer of charges at the electrode/electrolyte interface.[1−3] EDLC electrode materials should have a high surface area for charge accumulation and a porous structure for efficient electrolyte access. Certain electrolytes cannot easily diffuse into disordered micropores of activated carbons, limiting their performance.[4] Therefore, controlling the mesoporosity is important, such that mesoporous carbon materials are attracting increasing interest.[5−7] Mesopores in carbon materials allow faster ion diffusion at high current densities with more efficient use of the surface area for the generation of electrical double layers. Two-dimensional (2D) mesoporous carbons may have shorter channels for charge transport,[8,9] which would be highly desirable for EDLCs. Mesoporous carbon materials have been obtained via a variety of methods including templating, which may produce ordered mesopores with narrow pore size distribution.[10,11] Recently, we established a templating process that involves metal carbide (LaC_2, CaC_2, YC_2) intermediates to form graphitic carbon.[12−14] At temperatures above 500 °C, carbon is formed by passing steam and acetylene gas over the metal carbide. Hydrolyzable carbides have been known since 1837.[15] It was later discovered that water could hydrolyze carbides of group 1 and 2 metals, as well as aluminum carbides, and rare-earth carbides.[16−18] In particular, magnesium oxide is capable of forming hydrolyzable carbides and is potentially a good template for the synthesis of porous carbons. MgO also can be easily removed from carbon products using dilute hydrochloric acid and recycled.[19]

Herein, we report hexagonal-shaped $Mg(OH)_2$ sheets that serve as a template for the synthesis of mesoporous hexagonal carbon sheets (MHCSs) using acetylene and steam. In this process, the $Mg(OH)_2$ has multiple functions and serves as a graphitization catalyst, 2D template, and pore-forming agent. The MHCSs showed a high specific surface area of 1785 $m^2 \cdot g^{-1}$ with a hierarchical pore size distribution. The MHCS-based electrode showed excellent performance in EDLC supercapacitors with a specific capacitance of 162 $F \cdot g^{-1}$. Furthermore, after 10,000 cycles of rapid charge/discharge at 10 $A \cdot g^{-1}$, an electrochemical stability of 87% retention was observed.

2. EXPERIMENTAL SECTION

All reagents were utilized as received without further purification. Magnesium hydroxide ($Mg(OH)_2$) was purchased from Mallinckrodt. Pluronic P123 (poly(ethylene glycol)-

Received: February 25, 2022
Accepted: June 20, 2022
Published: June 29, 2022

https://doi.org/10.1021/acsomega.2c01149
ACS Omega 2022, 7, 27896−27902

block-poly(propylene glycol)-*block*-poly(ethylene glycol)) and 1-ethyl-3-methylimidazolium bis(trifluoromethylsulfonyl)-imide (EMIM-TFSI) were obtained from Sigma-Aldrich. Acetylene and ultrahigh purity nitrogen were obtained from Airgas.

2.1. Synthesis of $Mg(OH)_2$. The $Mg(OH)_2$ hexagons were synthesized by a hydrothermal method utilizing magnesium hydroxide and P123 surfactant.[20] In a typical synthesis, 0.3 g of $Mg(OH)_2$ and 0.5 g of P123 were added to 30 mL of deionized water and stirred at room temperature for 12 h. The solution was then transferred to a 45 mL Teflon-lined autoclave and heated at 180 °C for 24 h. After cooling to room temperature, the $Mg(OH)_2$ white powder was washed with deionized water and 200 proof ethanol, then dried at 80 °C for 12 h under vacuum. The $Mg(OH)_2$ hexagons were converted to MgO before the CVD process by heating to 650 °C at 1−2 °C/min. This was maintained for 18 min and then cooled down to room temperature under ultrahigh purity nitrogen. The sample was named magnesium oxide hexagon.

2.2. Synthesis of MHCS Carbon. The magnesium hydroxide hexagon-templated carbon sheets (MHCSs) were prepared by chemical vapor deposition using steam and acetylene. The magnesium hydroxide powder in a ceramic boat was placed at the center of a 2 inch horizontal quartz tube. The standard synthesis protocol is shown in Figure S1. Before the CVD process, the $Mg(OH)_2$ template was annealed under ultrahigh purity (99.999%) nitrogen at 1−2 °C/min to prevent the structure from collapsing and to preserve the morphology of the $Mg(OH)_2$.[21] Then, at 650 °C for 18 min, a flow of acetylene (30 cm^3/min) and steam (0.5 mL/h) was added. After the CVD procedure, the acetylene and steam flow was discontinued, and the temperature was increased to 900 °C at 5 °C/min and maintained for 2 h under N_2 for graphitization. During the high-temperature annealing, magnesium hydroxide was converted to magnesium oxide. After the furnace cooled down to room temperature, the magnesium oxide template was removed with dilute hydrochloric acid. The resulting black powder was separated by centrifugation and rinsed with deionized water and 100% ethanol. The final product was vacuum-dried at 80 °C.

2.3. Characterizations. The powder X-ray diffraction patterns of the samples were obtained with a Rigaku Ultima IV diffractometer (Cu Kα radiation). The composition of the surface elements was determined by X-ray photoelectron spectroscopy measurements using a PHI VersaProbe II. The photoelectrons were generated with monochromatic Al Kα radiation ($h\nu$ = 1486.6 eV), and the spectra were collected incident to the sample in the hemispherical analyzer with 0.2 eV step size and a pass energy of 28.5 eV. Raman spectra were obtained with a Thermo Scientific DXR Raman microscope with a laser excitation wavelength of 532 nm. The morphology was characterized by transmission electron microscopy (JEOL JEM-2100 TEM) at 200 kV. The porosity properties were measured with a Micromeritics ASAP 2020 via the nitrogen adsorption−desorption isotherms at 77 K. The specific surface area was determined by the Brunauer−Emmett−Teller (BET) method. Pore size distribution was determined by the two-dimensional nonlinear density functional theory (2D NLDFT) method.

2.4. Electrochemical Measurements. The MHCS powder was mixed with 5 wt % polytetrafluoroethylene (PTFE) binder and rolled into a film with a thickness of 100 μm, which was then punched into 11 mm-diameter circular disks. A CR2032-type symmetric capacitor was assembled with a PTFE (Gore) separator and EMIM-TFSI as electrolyte. All electrochemical measurements were carried out on an Arbin supercapacitor testing system (SCTS). Cyclic voltammetry (CV) measurements were taken in a voltage window ranging from −2.0 and 2.0 V, with scan rates from 5 to 100 mV s^{-1}. Galvanostatic charge−discharge (GCD) cycles were performed with voltages of 0 V and 3.5 V at current densities from 0.5 to 10 A·g^{-1}. Electrochemical impedance spectroscopy (EIS) analysis was conducted at an open-circuit voltage with a frequency range of 100 kHz to 10 mHz and with an amplitude of 10 mV using a 2273A Applied Research potentiostat/galvanostat (Princeton). The gravimetric specific capacitance (C_{sp}, F·g^{-1}) of the electrode, the gravimetric energy density (E, Wh·kg^{-1}), and the power density (P, kW·g^{-1}) of the supercapacitor were determined from the discharge curve of a GCD cycle using the following equations

$$C_{sp} = \frac{4I\Delta t}{m\Delta V} \quad (1)$$

$$E(\mathrm{Wh/kg}) = \frac{CspV^2}{7.2} \quad (2)$$

$$P(\mathrm{kW/kg}) = \frac{E \times 3600}{\Delta t} \quad (3)$$

where I (A) denotes the discharge current, Δt (s) and ΔV (V) denote the discharge time and voltage window, respectively, after subtracting the initial ohmic (IR) drop, and m (g) denotes the total mass of the electrode materials.

3. RESULTS AND DISCUSSION

As illustrated in Figure 1, the MHCS was synthesized via chemical vapor deposition (CVD) on a magnesium hydroxide $Mg(OH)_2$ template using acetylene and steam.

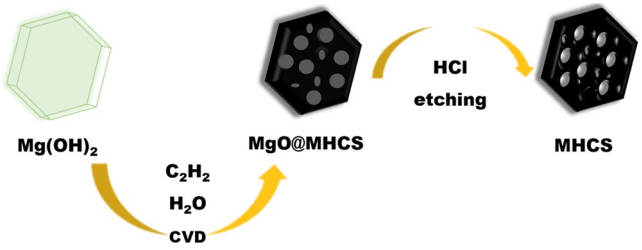

Figure 1. Illustration of the synthesis of the mesoporous hexagonal carbon sheet.

Based on previous studies,[12−14] a mechanism for this reaction is proposed below

$$2MgO + 3C_2H_2 \xrightarrow{\Delta} 2MgC_2 + 2CO + 3H_2\uparrow \quad (4)$$

$$2MgC_2 + 4H_2O \xrightarrow{\Delta} 2Mg(OH)_2 + 4C + 2H_2\uparrow \quad (5)$$

$$2MgO + 4H_2O + 3C_2H_2 \xrightarrow{\Delta} 2Mg(OH)_2 + 4C + 2CO\uparrow + 5H_2\uparrow \quad (6)$$

Equation 4 shows that the oxygen in MgO reacts with acetylene to form CO, leaving the magnesium to form a carbide. When the steam was supplied, magnesium acetylide was hydrolyzed to $Mg(OH)_2$ and acetylene anions C^{2-}. The

https://doi.org/10.1021/acsomega.2c01149
ACS Omega 2022, 7, 27896−27902

C^{2-}underwent polymerization, followed by graphitization at 900 °C, as shown in eq 5. Equation 6 shows the overall reaction.

Figure 2a shows that the $Mg(OH)_2$ templates are composed of free-standing hexagonal-shaped sheets with diameters

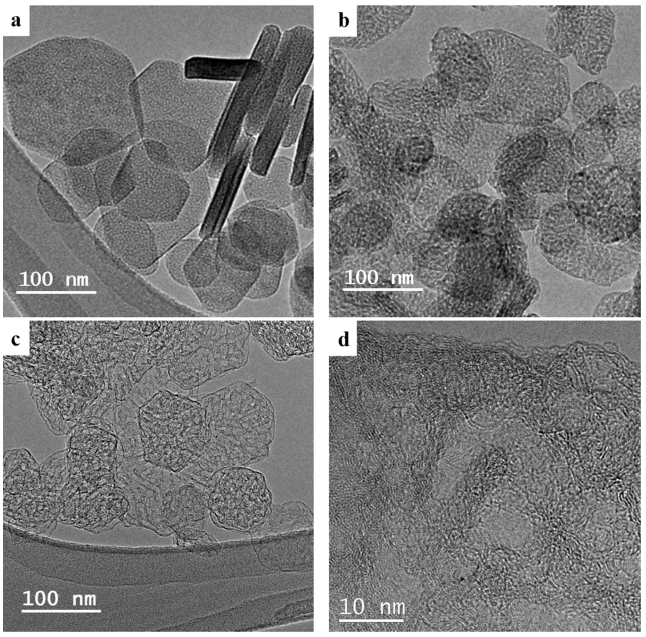

Figure 2. TEM images: (a) magnesium hydroxide, (b) magnesium hydroxide after annealing at 650 °C, and (c, d) mesoporous hexagonal carbon sheet (MHCS).

ranging from 40 to 100 nm. Some hexagonal sheets are perpendicular to the plane of view, showing a thickness of 10−25 nm. After annealing at 650 °C, the magnesium hydroxide transforms into magnesium oxide by losing water, which acts as a porogen, as shown in Figure 2b. After the CVD and removal of the MgO template, the resulting MHCS is shown in Figure 2c,d. The hexagonal shape is preserved with mesopores around 5 nm in diameter. The porous carbon material's distinctive structure is critical for good performance, by allowing electrolyte ion diffusion into the carbon structure.[22] Obvious graphitic fringes with a *d*-spacing of 0.39 nm were observed in the HRTEM images, as shown in Figure 2d.

The $Mg(OH)_2$ hexagonal sheets clearly show the XRD patterns of crystalline $Mg(OH)_2$ (JCPDS 7-0239), as shown in Figure 3.[23] After the carbon deposition, the XRD pattern mainly exhibits the sharp diffraction peaks of MgO (JCPDS 01-075-c0447).[23] After the removal of the MgO template, the MHCS shows two broad peaks around 23.2° (002) and the reflections of the weak (101) faces at 43°.[24] The *d*-spacing calculated was 0.39 nm, which matches the lattice spacing from TEM images. The mean crystalline size (Lc) calculated from the broadened (002) peak was 3.8 nm, indicating that the hexagonal carbon sheets contain relatively small domains of stacked crystalline graphite.[25,26]

Figure 4a shows the deconvoluted Raman spectrum for the MHCS. The D band at the 1340 cm^{-1} peak corresponds to the disorder caused by the lattice distortion. While the 1590 cm^{-1} peak of the G band is indicative of the C−C stretching vibration of sp^2-hybridized carbon atoms in rings and chains.[27] The D3 band at 1500 cm^{-1} between the two peak maxima originates from the amorphous carbon.[28] The relative intensity

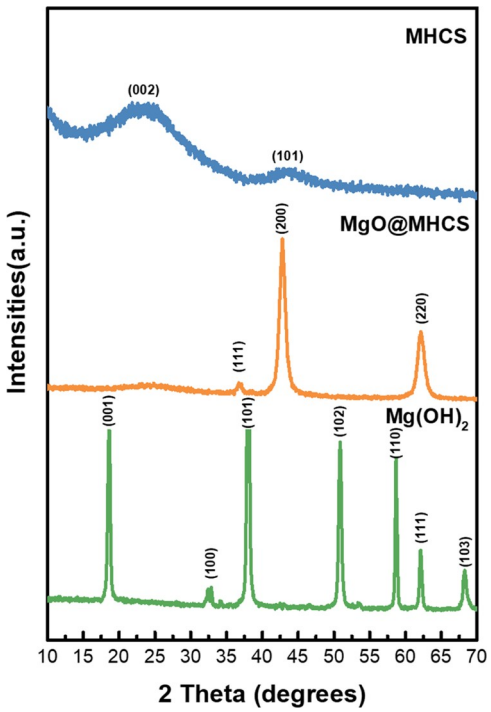

Figure 3. Powder X-ray diffraction patterns of $Mg(OH)_2$, MgO/MHCS, and MHCS.

ratio (I_D/I_G) of the D band to the G band of the carbon material is proportional to the degree of graphitization, and the MHCS has an I_D/I_G of 1.07 with a domain size L_a of 4.11 nm.[29,30] The templated carbon derived from lanthanum hydroxide nanorod and yttrium hydroxide templates also showed a broad D band for disordered defects.[12,14]

The surface composition of the MHCS was characterized by XPS. Figures S3 and 4b show the survey spectrum and C 1s spectrum after background subtraction using Shirley's method, respectively.[31] The oxygen to carbon content ratio is 4.97:95.03. Because oxygen species have a lower tolerance than sp^2 carbon at high voltage and their detrimental effect on the $\pi-\pi$ configuration in sp^2 carbon, the high purity proved helpful for increasing the cycling performance and the charge transfer rate.[32] The C 1s spectrum was deconvoluted into five Gaussian curves, which correspond to the C−C, C−O, C═O, and O−C═O bonds and a $\pi-\pi^*$ transition satellite peak at 290.3 eV, indicating a strong $\pi-\pi^*$ stacking from aromatic carbons and facilitates electron transfer.[32,33] The conductivity of MHCS measured by a four-point probe method was 5.237×10^3 $S{\cdot}m^{-1}$, which is comparable to that of calcium hydroxide and yttrium hydroxide-templated carbons.[12,14]

Figures 5a and S4 show the N_2 adsorption−desorption isotherms of the $Mg(OH)_2$, the MgO after annealing, and the MHCS. The $Mg(OH)_2$ exhibits a type II isotherm with a surface area of 34 $m^2{\cdot}g^{-1}$, indicating that the only porosity was space between hexagonal sheets.[34] During the heating process, the $Mg(OH)_2$ template loses water to form MgO, and the specific surface area of MgO increases to 115 $m^2{\cdot}g^{-1}$. After removal of the MgO template, the MHCS exhibits a type IV isotherm, as shown in Figure 5a, which corresponds to a mesoporous structure with a distinct hysteresis between the 0.4 and 1.0 relative pressure.[35] Additionally, the adsorption knee below 0.1 also shows some microporosity. The corresponding 2D NLDFT pore size distribution shows that the hierarchical

https://doi.org/10.1021/acsomega.2c01149
ACS Omega 2022, 7, 27896−27902

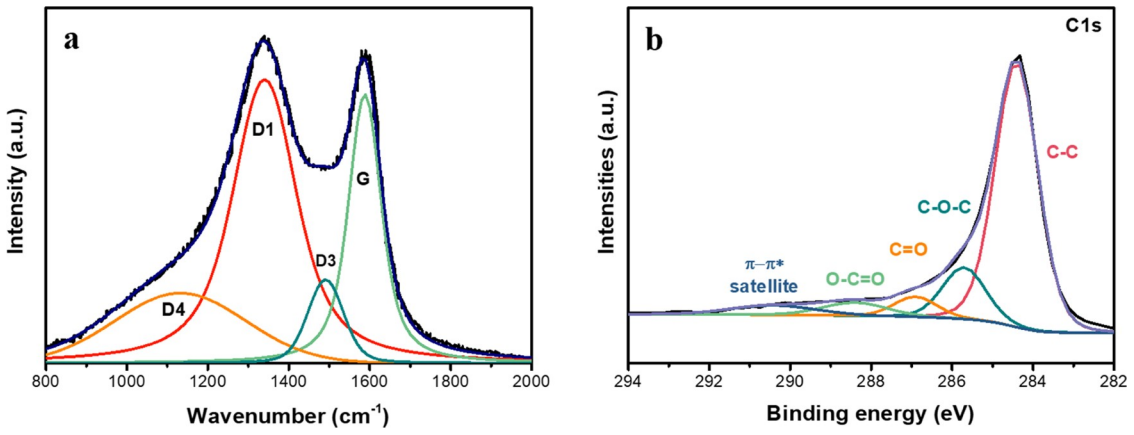

Figure 4. (a) Raman spectrum of MHCS; (b) high-resolution C 1s spectrum of MHCS.

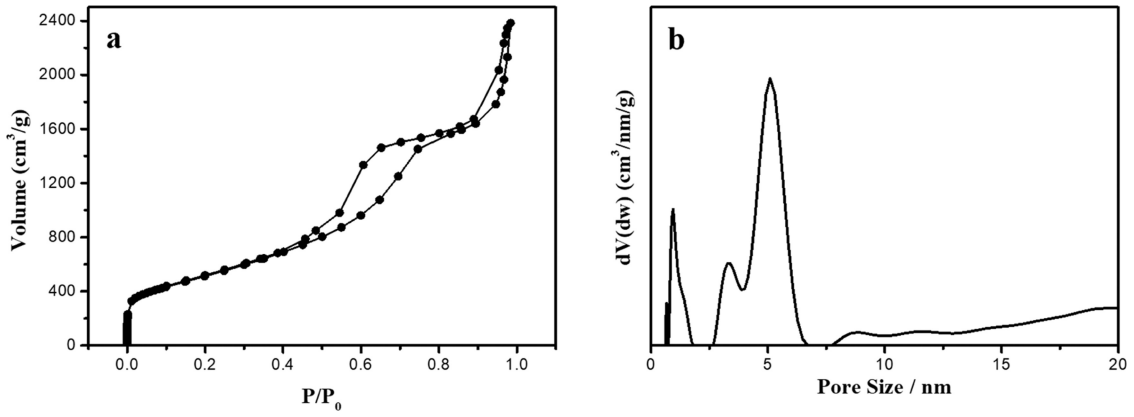

Figure 5. (a) N_2 adsorption−desorption isotherms of MHCS; (b) two-dimensional nonlinear density functional theory (2D NLDFT) pore size distribution of MHCS.

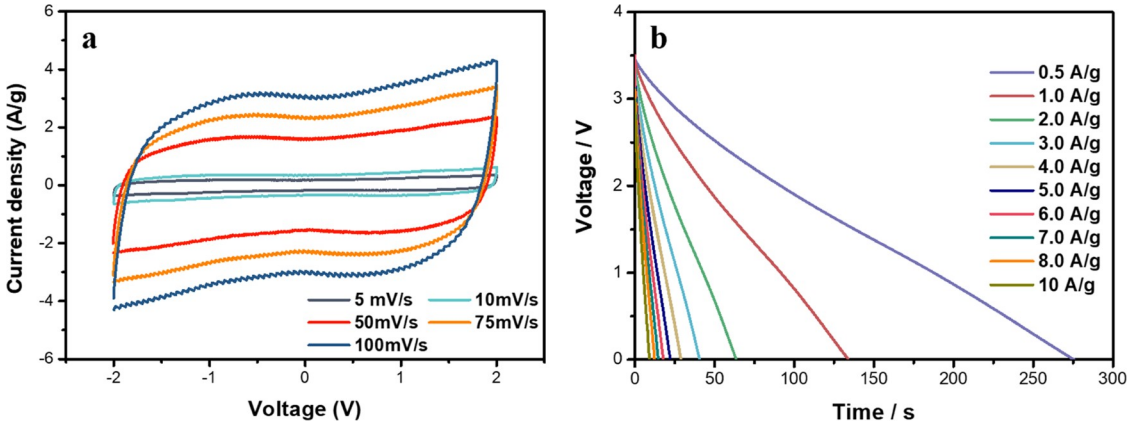

Figure 6. Electrochemical characterizations of MHCS: (a) cyclic voltammograms; (b) discharge curves from 0.5 to 10 $A{\cdot}g^{-1}$.

pore size systems consist of micropores mainly centered at 0.69 nm and 0.95 nm, as well as mesopore systems around 3.38 nm and 5.10 nm, which is consistent with TEM images. Due to the large degree of structural porosity, the MHCS has a high surface area of 1785 $m^2{\cdot}g^{-1}$. Notably, the mesopore volume in MHCS is up to 3.485 $cm^3{\cdot}g^{-1}$, accounting for 97% of the total pore volume of 3.583 $cm^3{\cdot}g^{-1}$. Due to the lower conductivity and high viscosity of ionic liquid electrolytes, micropores (less than 2 nm) contribute to the maximum capacitance, but rate performance is limited. The mesopores in the MHCS would promote the fast ion transport for ionic liquid electrolytes, such as EMIM-TFSI.[36]

The electrochemical performance of MHCS electrodes was assessed utilizing a symmetric two-electrode configuration with EMIM-TFSI as the electrolyte. The electrochemical behavior of the supercapacitors was evaluated by cyclic voltammetry (CV), galvanostatic discharge−charge (GCD), electrochemical impedance spectroscopy (EIS), and cycling tests. Figure 6a shows the CV curve of the MHCS at different scan rates in the range of −2.0 to 2.0 V. The rectangular shape of the CV indicates ideal electrical double layer capacitive behavior.[37]

https://doi.org/10.1021/acsomega.2c01149
ACS Omega 2022, 7, 27896−27902

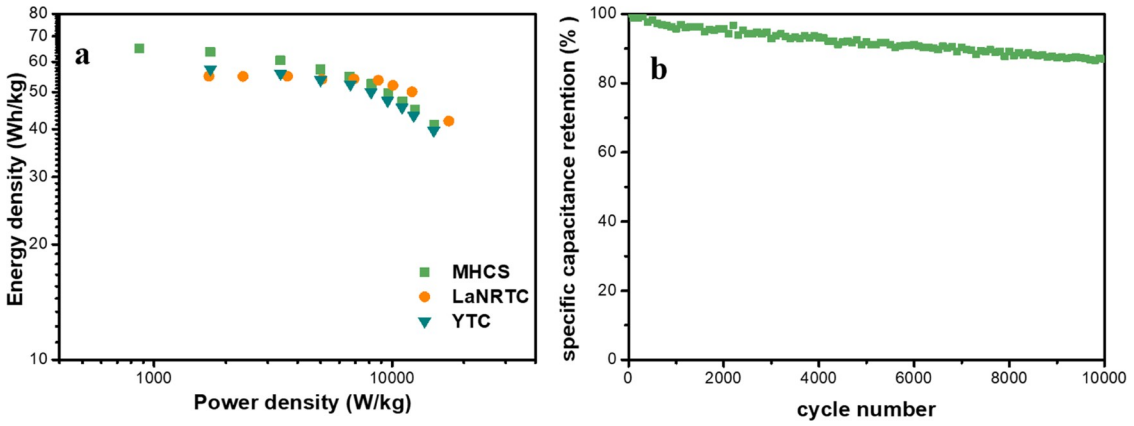

Figure 7. (a) Ragone plot; (b) cycling performance at 10 A·g^{-1}.

The rectangular shape is maintained when the scan rate is increased from 5 to 100 mV·s^{-1}, exhibiting good capacitive performance at high scan rates for rapid electrolyte transport within the electrodes and also good charge diffusion of ions at the electrolyte−carbon material interfaces. The highest specific capacitance was obtained at 5 mV/s as 162 F·g^{-1}, which is significantly higher than the specific capacitance of 128 F·g^{-1} for $La(OH)_3$ nanorod-templated carbon (LaNRTC), 135 F·g^{-1} acquired from asphaltene-based porous carbon nanosheets, and 137 F·g^{-1} for $Y(OH)_3$-templated carbon (YTC).[12,14,38] The specific capacitance was 125 F·g^{-1} at 100 mV/s, showing good rate performance.

The discharge curves of GCD measurement are shown in Figure 6b. The calculated specific capacitances were 161, 157, 151, 147, 142, 138, 135, 133, 128, and 124 F·g^{-1} under the current densities of 0.5, 1, 2, 3, 4, 5, 6, 7, 8, and 10 A·g^{-1}, respectively. It is worth noting that when the current density is increased to 10 A·g^{-1}, the specific capacitance maintains at 77% of its initial value at 0.5 A·g^{-1}. The GCD curves recorded at 0.5 A·g^{-1} exhibited a nearly straight line with a small IR drop, indicating the superior reversible electrochemical performance.

The Ragone plot in Figure 7a shows the highest energy density of 67 Wh·kg^{-1} at 0.5 A·g^{-1} with a power density of 866 W·kg^{-1}. Furthermore, even at a high power density of 14.97 kW·kg^{-1} at 10 A·g^{-1}, the MHCS still delivers an energy density of 38 Wh·kg^{-1}. These results show the MHCS's highly integrated power-energy qualities are comparable to those of other templated carbons, such as LaNRTC (55 Wh·kg^{-1} with 1.7 kW·kg^{-1} at 1.0 A·g^{-1}) and YTC (57.4 Wh·kg^{-1} with 1.724 kW·kg^{-1} at 1.0 A·g^{-1}).

Charge−discharge measurements at 10 A·g^{-1} were used to assess the electrochemical cycling stability of MHCS-based supercapacitors, as shown in Figure 7b. After 10,000 cycles, MHCS exhibits a minor loss of capacitance, with an 87% retention rate.

The EIS result obtained in the frequency range of 1 MHz to 10 mHz (Figure 8) shows a steep increase at a low frequency, which is a distinctive feature of capacitive behavior.[39] The semicircle at a high frequency revealed a low charge transfer resistance (R_{ct}) of 3.77 Ω, showing the fast ion diffusion and the excellent electrical conductivity, compared to LaNRTC with 4 Ω and YTC with 26.3 Ω. According to the *x*-intercept, the solution resistance (R_s) was only 3 Ω, which is also smaller than those for LaNRTC with 3.4 Ω and YTC with 7.9 Ω.[12,14]

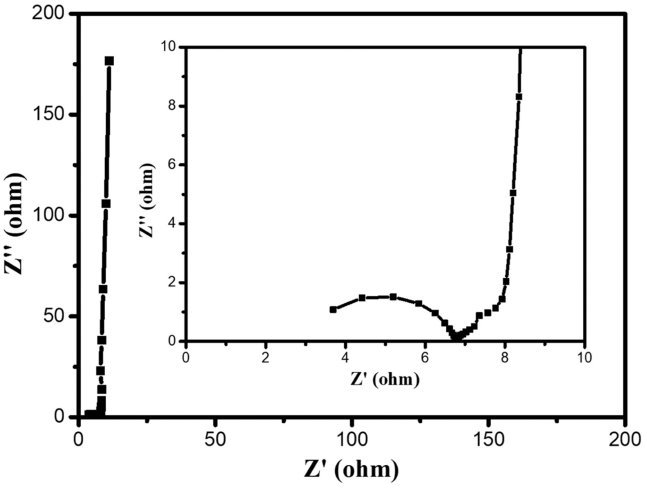

Figure 8. Electrochemical impedance spectrum (EIS) of MHCS.

The combination of the mesoporous structure and wide operating voltage of the IL electrolyte enables the high power and energy density properties of the MHCS supercapacitors. The mesoporosity of MHCS facilitates electrolyte ions to diffuse into electrode material pores, driving the formation of the electrical double layer and enhancing specific capacitance.

4. CONCLUSIONS

In conclusion, we presented an efficient approach for producing mesoporous hexagonal carbon sheets (MHCSs) with a controllable pore size distribution. The MHCS with interconnected mesopores showed a high specific surface area (SSA) of 1785 m^2·g^{-1}. This high SSA of MHCS contributes to the high EDL capacitance, while the mesoporous structure guarantees that the internal surface is accessible to the ionic liquid electrolyte. This results in a high energy density of 67 Wh·kg^{-1} at 866 W·kg^{-1} and a high rate capability of 38 Wh·kg^{-1} at 14.97 kW·kg^{-1}. Meanwhile, the $Mg(OH)_2$ template is more cost-effective than $La(OH)_3$ and $Y(OH)_3$, which facilitates large-scale production.

■ ASSOCIATED CONTENT

Supporting Information

The Supporting Information is available free of charge at https://pubs.acs.org/doi/10.1021/acsomega.2c01149.

https://doi.org/10.1021/acsomega.2c01149
ACS Omega 2022, 7, 27896−27902

XPS survey spectrum of MHCS; N_2 adsorption/desorption isotherms and summary of the pore size distribution of $Mg(OH)_2$ and MgO; textural properties of $Mg(OH)_2$, MgO, and MHCS; specific capacitances under different scan rates; and energy and power densities (PDF)

AUTHOR INFORMATION

Corresponding Author

Kenneth J. Balkus, Jr. − *Department of Chemistry and Biochemistry, The University of Texas at Dallas, Richardson, Texas 75080, United States;* orcid.org/0000-0003-1142-3837; Email: balkus@utdallas.edu

Authors

Yafen Tian − *Department of Chemistry and Biochemistry, The University of Texas at Dallas, Richardson, Texas 75080, United States;* orcid.org/0000-0001-5048-8663

Xiangyu Zhu − *Department of Materials Science and Engineering, The University of Texas at Dallas, Richardson, Texas 75080, United States*

Muhammad Abbas − *Department of Chemistry and Biochemistry, The University of Texas at Dallas, Richardson, Texas 75080, United States;* orcid.org/0000-0001-6950-8986

Daniel W. Tague − *Department of Chemistry and Biochemistry, The University of Texas at Dallas, Richardson, Texas 75080, United States*

John P. Ferraris − *Department of Chemistry and Biochemistry, The University of Texas at Dallas, Richardson, Texas 75080, United States;* orcid.org/0000-0002-3225-0093

Complete contact information is available at: https://pubs.acs.org/10.1021/acsomega.2c01149

Notes

The authors declare no competing financial interest.

ACKNOWLEDGMENTS

The authors acknowledge the Robert A. Welch Foundation (AT-1153) for financial support. This project also was partially funded by The University of Texas at Dallas Office of Research through the Core Facility Voucher Program (10319). Syed Fahad Bin Haque is acknowledged for performing SEM analysis.

REFERENCES

(1) Gu, W.; Yushin, G. Review of Nanostructured Carbon Materials for Electrochemical Capacitor Applications: Advantages and Limitations of Activated Carbon, Carbide-Derived Carbon, Zeolite-Templated Carbon, Carbon Aerogels, Carbon Nanotubes, Onion-like Carbon, and Graphene. *Wiley Interdiscip. Rev. Energy Environ.* **2014**, *3*, 424−473.

(2) Wang, Y.; Zhang, L.; Hou, H.; Xu, W.; Duan, G.; He, S.; Liu, K.; Jiang, S. Recent Progress in Carbon-Based Materials for Supercapacitor Electrodes: A Review. *J. Mater. Sci.* **2021**, *56*, 173−200.

(3) Wang, Y.; Song, Y.; Xia, Y. Electrochemical Capacitors: Mechanism, Materials, Systems, Characterization and Applications. *Chem. Soc. Rev.* **2016**, *45*, 5925−5950.

(4) Shi, H. Activated Carbons and Double Layer Capacitance. *Electrochim. Acta* **1996**, *41*, 1633−1639.

(5) Rahman, M. M.; Ara, M. G.; Alim, M. A.; Uddin, M. S.; Najda, A.; Albadrani, G. M.; Sayed, A. A.; Mousa, S. A.; Abdel-Daim, M. M. Mesoporous Carbon: A Versatile Material for Scientific Applications. *Int. J. Mol. Sci.* **2021**, *22*, 4498.

(6) Wu, F.; Li, J.; Tian, Y.; Su, Y.; Wang, J.; Yang, W.; Li, N.; Chen, S.; Bao, L. 3D Coral-like Nitrogen-Sulfur Co-Doped Carbon-Sulfur Composite for High Performance Lithium-Sulfur Batteries. *Sci. Rep.* **2015**, *5*, No. 13340.

(7) Yang, C.; Zhu, X.; Wang, X.; Wang, J.; Huang, H. Phase-Field Model of Graphene Aerogel Formation by Ice Template Method. *Appl. Phys. Lett.* **2019**, *115*, No. 111901.

(8) Tang, Q.; Bairi, P.; Shrestha, R. G.; Hill, J. P.; Ariga, K.; Zeng, H.; Ji, Q.; Shrestha, L. K. Quasi 2D Mesoporous Carbon Microbelts Derived from Fullerene Crystals as an Electrode Material for Electrochemical Supercapacitors. *ACS Appl. Mater. Interfaces* **2017**, *9*, 44458−44465.

(9) Yang, W.; Ni, M.; Ren, X.; Tian, Y.; Li, N.; Su, Y.; Zhang, X. Graphene in Supercapacitor Applications. *Curr. Opin. Colloid Interface Sci.* **2015**, *20*, 416−428.

(10) Xin, W.; Song, Y. Mesoporous Carbons: Recent Advances in Synthesis and Typical Applications. *RSC Adv.* **2015**, *5*, 83239−83285.

(11) Zhu, X.; Yang, C.; Wu, P.; Ma, Z.; Shang, Y.; Bai, G.; Liu, X.; Chang, G.; Li, N.; Dai, J.; Wang, X.; Zhang, H. Precise Control of Versatile Microstructure and Properties of Graphene Aerogel: Via Freezing Manipulation. *Nanoscale* **2020**, *12*, 4882−4894.

(12) Wang, Z.; Perera, W. A.; Perananthan, S.; Ferraris, J. P.; Balkus, K. J. Lanthanum Hydroxide Nanorod-Templated Graphitic Hollow Carbon Nanorods for Supercapacitors. *ACS Omega* **2018**, *3*, 13913−13918.

(13) Brown, A. T.; Lin, J.; P Vizuet, J.; C Thomas, M.; J Balkus, K. Graphene-like Carbon from Calcium Hydroxide. *ACS Omega* **2021**, *6*, 31066−31076.

(14) Brown, A. T.; Agrawal, V. S.; Wunch, M. A.; Lin, J.; Thomas, M. C.; Ferraris, J. P.; Chabal, Y. J.; Balkus, K. J. Yttrium Oxide-Catalyzed Formation of Electrically Conductive Carbon for Supercapacitors. *ACS Appl. Energy Mater.* **2021**, *4*, 12499−12507.

(15) Wisniak, J. The History of Catalysis. From the Beginning to Nobel Prizes. *Educ. Quim.* **2010**, *21*, 60−69.

(16) Pring, J. N. CCX. - The Formation of Some Carbides. *J. Chem. Soc., Trans.* **1908**, *93*, 2101−2108.

(17) Rueggeberg, W. H. C. The Carbides of Magnesium. *J. Am. Chem. Soc.* **1943**, *65*, 602−607.

(18) Hajek, B.; Karen, P.; Brozek, V. Hydrolyzable Carbides: Relationships between Their Structure and the Composition of Their Hydrolysis Products. *Rev. Inorg. Chem.* **1986**, *8*, 117−160.

(19) Morishita, T.; Tsumura, T.; Toyoda, M.; Przepiórski, J.; Morawski, A. W.; Konno, H.; Inagaki, M. A Review of the Control of Pore Structure in MgO-Templated Nanoporous Carbons. *Carbon* **2010**, *48*, 2690−2707.

(20) Balducci, G.; Bravo Diaz, L.; Gregory, D. H. Recent Progress in the Synthesis of Nanostructured Magnesium Hydroxide. *CrystEngComm* **2017**, *19*, 6067−6084.

(21) Ding, Y.; Zhang, G.; Wu, H.; Hai, B.; Wang, L.; Qian, Y. Nanoscale magnesium hydroxide and magnesium oxide powders: control over size, shape, and structure via hydrothermal synthesis. *Chem. Mater.* **2001**, *13*, 435−440.

(22) Wang, J. G.; Liu, H.; Sun, H.; Hua, W.; Wang, H.; Liu, X.; Wei, B. One-Pot Synthesis of Nitrogen-Doped Ordered Mesoporous Carbon Spheres for High-Rate and Long-Cycle Life Supercapacitors. *Carbon* **2018**, *127*, 85−92.

(23) Yousefi, S.; Ghasemi, B.; Tajally, M.; Asghari, A. Optical Properties of MgO and $Mg(OH)_2$ Nanostructures Synthesized by a Chemical Precipitation Method Using Impure Brine. *J. Alloys Compd.* **2017**, *711*, 521−529.

(24) Shao, M.; Wang, D.; Yu, G.; Hu, B.; Yu, W.; Qian, Y. The synthesis of carbon nanotubes at low temperature via carbon suboxide disproportionation. *Carbon* **2004**, *42*, 183−185.

(25) Milev, A.; Wilson, M.; Kannangara, G. S. K.; Tran, N. X-Ray Diffraction Line Profile Analysis of Nanocrystalline Graphite. *Mater Chem. Phys.* **2008**, *111*, 346−350.

https://doi.org/10.1021/acsomega.2c01149
ACS Omega 2022, 7, 27896−27902

(26) Maurin, G.; Stepanek, I.; Bernier, P.; Colomer, J. F.; Nagy, J. B.; Henn, F. Segmented and opened multi-walled carbon nanotubes. *Carbon* **2001**, *39*, 1273−1278.
(27) Kaniyoor, A.; Ramaprabhu, S. A Raman Spectroscopic Investigation of Graphite Oxide Derived Graphene. *AIP Adv.* **2012**, *2*, No. 032183.
(28) Sadezky, A.; Muckenhuber, H.; Grothe, H.; Niessner, R.; Pöschl, U. Raman Microspectroscopy of Soot and Related Carbonaceous Materials: Spectral Analysis and Structural Information. *Carbon* **2005**, *43*, 1731−1742.
(29) Maslova, O. A.; Ammar, M. R.; Guimbretière, G.; Rouzaud, J. N.; Simon, P. Determination of Crystallite Size in Polished Graphitized Carbon by Raman Spectroscopy. *Phys. Rev. B* **2012**, *86*, No. 134205.
(30) Ferrari, A. C.; Robertson, J. Interpretation of Raman Spectra of Disordered and Amorphous Carbon. *Phys. Rev. B* **2000**, *61*, 14095.
(31) Shinotsuka, H.; Yoshikawa, H.; Murakami, R.; Nakamura, K.; Tanaka, H.; Yoshihara, K. Automated Peak Fitting of XPS Spectrum Using Information Criteria. *J. Surf. Anal.* **2019**, *26*, 126−127.
(32) Bosch-Navarro, C.; Busolo, F.; Coronado, E.; Duan, Y.; Martí-Gastaldo, C.; Prima-Garcia, H. Influence of the Covalent Grafting of Organic Radicals to Graphene on Its Magnetoresistance. *J. Mater. Chem. C* **2013**, *1*, 4590−4598.
(33) Cheng, W.; Weng, L. T.; Li, Y.; Lau, A.; Chan, C. K.; Chan, C. M. Surface Chemical Composition of Size-Fractionated Urban Walkway Aerosols Determined by x-Ray Photoelectron Spectroscopy. *Aerosol Sci. Technol.* **2013**, *47*, 1118−1124.
(34) Awe, A. A.; Opeolu, B. O.; Fatoki, O. S.; Ayanda, O. S.; Jackson, V. A.; Snyman, R. Preparation and Characterisation of Activated Carbon from Vitis Vinifera Leaf Litter and Its Adsorption Performance for Aqueous Phenanthrene. *Appl. Biol. Chem.* **2020**, *63*, 12.
(35) Wahab, M. A.; Darain, F.; Karim, M. A.; Beltramini, J. N. Nano-Confined Synthesis of Highly Ordered Mesoporous Carbon and Its Performance as Electrode Material for Electrochemical Behavior of Riboflavin (Vitamin B2) and Dopamine. *Int. J. Electrochem. Sci.* **2015**, *10*, 7732−7742.
(36) Lazzari, M.; Soavi, F.; Mastragostino, M. Mesoporous Carbon Design for Ionic Liquid-Based, Double-Layer Supercapacitors. *Fuel Cells* **2010**, *10*, 840−847.
(37) Frackowiak, E.; Béguin, F. Electrochemical Storage of Energy in Carbon Nanotubes and Nanostructured Carbons. *Carbon* **2002**, *40*, 1775−1787.
(38) Qin, F.; Tian, X.; Guo, Z.; Shen, W. Asphaltene-Based Porous Carbon Nanosheet as Electrode for Supercapacitor. *ACS Sustainable Chem. Eng.* **2018**, *6*, 15708−15719.
(39) Mei, B. A.; Munteshari, O.; Lau, J.; Dunn, B.; Pilon, L. Physical Interpretations of Nyquist Plots for EDLC Electrodes and Devices. *J. Phys. Chem. C* **2018**, *122*, 194−206.

https://doi.org/10.1021/acsomega.2c01149
ACS Omega 2022, 7, 27896−27902